eJSSNT Regular Paper

e-Journal of Surface Science and Nanotechnology **23**, 36–43 (2025)

A Voxel Method for Correcting the Self-absorption Effect in Fluorescence X-ray Absorption Fine Structure Spectra

Daisuke Shibata,[a, †] Toshiaki Ohta,[a] Yuki Orikasa,[b] Kimihiko Ito,[c] Kiyotaka Asakura [a, ‡]

[a] *SR Center, Research Organization of Science and Technology, Ritsumeikan University, 1-1-1 Noji-Higashi, Kusatsu, Shiga 525-8577, Japan*
[b] *College of Life Sciences, Ritsumeikan University, 1-1-1 Noji-Higashi, Kusatsu 525-8577, Japan*
[c] *National Institute for Materials Science, 1-2-1 Sengen, Tsukuba, Ibaraki 305-0047, Japan*
[†] *Corresponding author: dshibata@fc.ritsumei.ac.jp*
[‡] *Corresponding author: kytkaskr@fc.ritsumei.ac.jp*

Received: 15 November, 2024; Accepted: 27 January, 2025; J-STAGE Advance Publication: 1 March, 2025; Published: 1 March, 2025

Partial fluorescence yield X-ray absorption fine structure (PFY-XAFS) spectroscopy in the soft X-ray region is important for obtaining information about the bulk region of a sample. However, the self-absorption effect is a serious problem that causes distortions to the fine structure of PFY-XAFS spectra. This self-absorption can be analytically corrected for flat surfaces but not for arbitrary shapes such as those of particles in powders. In this study, we propose a voxel method where we divide the sample with arbitrary shapes into small boxes (called voxel) to calculate the self-absorption effect. By comparing the O K-edge PFY-XAFS spectra of a CoO single crystal, a thin layer Li_2CO_3 on a NiO substrate, and a CoO powder sample, we investigate the validity of the voxel method, along with its merits and limitations.

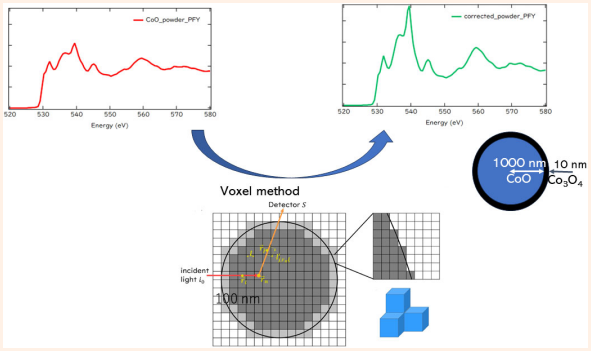

Keywords *Soft X-ray PFY-XAFS; Self-absorption; Voxel method*

I. INTRODUCTION

X-ray absorption fine structure (XAFS) spectroscopy is a powerful technique used to characterize the local structure and electronic states around X-ray-absorbing atoms in both crystalline and amorphous materials [1, 2]. The key feature of XAFS spectroscopy is its element specificity, which is possible because each element has a characteristic absorption edge energy. In particular, hard X-rays with an energy greater than 4 keV exhibit high penetration ability and allow XAFS experiments to be conducted in a transmission mode even under ambient conditions. Operando XAFS under high pressure provides information about catalyst chemical reaction mechanisms [3]. However, transmission-mode XAFS analysis of light elements, such as carbon, oxygen, and fluorine, is difficult because the K edges of these elements correspond to the soft X-ray region (<1000 eV), and soft X-rays have much less penetration ability than hard X-rays. The penetration ability is estimated by the attenuation length. For example, carbon materials, oxides, and fluorides typically have an attenuation length of 100, 280, or 350 nm, respectively, after the K-absorption edges [4]. Electron-based detection methods, such as total electron yield (TEY) and partial electron yield (PEY), are usually used in soft X-ray XAFS measurements [5, 6]. However, because these electron-yield detection methods are surface sensitive, the obtained spectra are strongly affected by the surface state, and obtaining information about the bulk region is difficult.

Partial fluorescence yield XAFS (PFY-XAFS) is an important method for obtaining XAFS information about low-concentration target elements in the bulk region of a sample. However, PFY-XAFS for concentrated samples suffers from a self-absorption effect, which reduces the intensity of the XAFS spectra and causes spectral distortion. For a flat substrate of uniform concentration with thickness d, the fluorescence intensity (I_F) including self-absorption can be obtained via the following analytical equation with incidence angle α and emission angle γ from the flat surface [see Figure 1(d)] [7–9]:

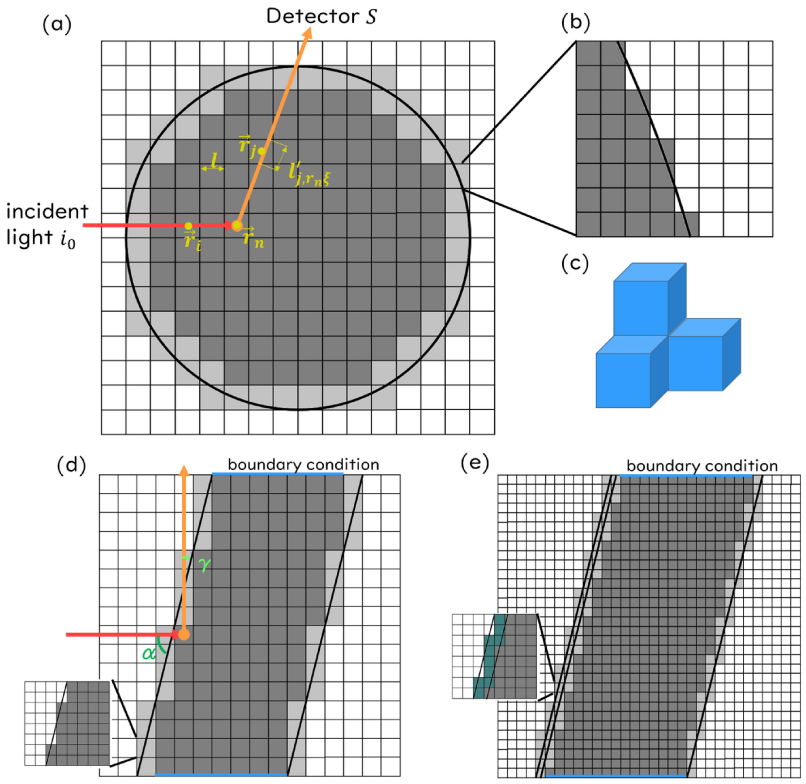

Figure 1: Schematic of (a) voxels and (b) subvoxels; dark and pale-gray boxes correspond to a full voxel and a border voxel, respectively. The border voxel is further divided into 8 × 8 × 8 subvoxels (b). (c) A three-dimensional drawing of a voxel. (d) CoO single crystal case. (e) Li_2CO_3/NiO film case; The green region in the subvoxel means Li_2CO_3 thin layer while the grey region in the subvoxel is the NiO substrate.

$$I_{\mathrm{F}} = \frac{k_X I_0 \mu_X(E)}{\mu_{\mathrm{tot}}(E) + \mu_{\mathrm{tot}}(E_{\mathrm{F}}) \frac{\sin\alpha}{\sin\gamma}} \times \left[1 - \exp\left(-\frac{\mu_{\mathrm{tot}}(E)}{\sin\alpha} d - \frac{\mu_{\mathrm{tot}}(E_{\mathrm{F}})}{\sin\gamma} d\right)\right], \quad (1)$$

where k_X, I_0, $\mu_X(E)$, $\mu_{\mathrm{tot}}(E)$, and $\mu_{\mathrm{tot}}(E_{\mathrm{F}})$ are the branching ratio of the fluorescence to Auger decays, the intensity of the incident X-rays, the X-ray absorption coefficient for the target X-ray absorption edge of the X-ray-absorbing atom X at incident X-ray energy E, the total absorption coefficient at E, and the total absorption coefficient at fluorescence X-ray energy E_{F}, respectively. The parameter $\mu_{\mathrm{tot}}(E)$ can be expressed as $\mu_{\mathrm{tot}}(E) = \mu_{\mathrm{BG}}(E) + \mu_X(E)$, where $\mu_{\mathrm{BG}}(E)$ is the background absorption coefficient at regions other than the target X-ray absorption edge for incident X-ray energy E. If the sample has a flat surface and the appropriate assumptions are made for μ_{BG} and $\mu_{\mathrm{tot}}(E_{\mathrm{F}})$, Eq. (1) can be used to estimate $\mu_X(E)$ from a spectrum, I_{F}/I_0, that is distorted by the self-absorption effect. We refer to fluorescence correction using Eq. (1) as the flat-surface model.

The thick samples have the term $1 - \exp\left(-\frac{\mu_{\mathrm{tot}}(E)}{\sin\alpha} d - \frac{\mu_{\mathrm{tot}}(E_{\mathrm{F}})}{\sin\gamma} d\right) \approx 1$. When $\mu_{\mathrm{BG}} \gg \mu_X$, Eq. (1) can be approximated as

$$I_{\mathrm{F}} = \frac{k_X I_0 \mu_X(E)}{\mu_{\mathrm{BG}}(E) + \mu_{\mathrm{tot}}(E_{\mathrm{F}}) \frac{\sin\alpha}{\sin\gamma}}. \quad (2)$$

Thus, $I_{\mathrm{F}}/I_0 \propto \mu_X(E)$. It is called as thick and dilute case in which the fluorescence XAFS works well without any corrections [10].

By contrast, in the thick and concentrated case,

$$I_{\mathrm{F}} = \frac{k_X I_0 \mu_X(E)}{\mu_{\mathrm{BG}}(E) + \mu_X(E) + \mu_{\mathrm{tot}}(E_{\mathrm{F}}) \frac{\sin\alpha}{\sin\gamma}}. \quad (3)$$

The μ_X terms in the numerator and denominator are canceled out, and the amplitude of the XAFS spectrum is reduced. The raw I_{F}/I_0 is not directly proportional to μ_X, and the self-absorption correction using Eq. (1) is necessary.

In the hard X-ray region, if the absorbance of the sample is not large (or if the attenuation length is sufficiently large), a flat surface can easily be obtained by compacting the powder into a disc. Creating a sufficiently flat surface in the soft X-ray region is difficult because the attenuation length is much smaller than that in the hard X-ray region and the surface roughness should be smaller than 100 nm. Consequently, applying the flat-surface model using Eq. (1) is not straightforward. In this article, we present the results of a new simulation method, referred to as the voxel method, in which the sample is divided into small cubes (voxels), and the self-absorption in each voxel is calculated to simulate μ_X for an arbitrarily shaped sample. In Section II, we describe the voxel method and the experimental details. In Section III, we check the validity of the voxel method in two ideal cases: a flat CoO single crystal and a flat thin Li_2CO_3 layer on a NiO substrate. Finally, we apply the voxel method to a powder system.

II. EXPERIMENTAL AND ANALYTICAL METHODS

A. XAFS measurements

The XAFS measurements were performed at beamline BL-11 at the SR Center, Ritsumeikan University (RSRC). The X-rays emitted from the ultra-compact storage ring Aurora-1 (Sumitomo Heavy Industry) operated at 150 mA with 0.575 GeV were monochromatized by a 1200 L mm^{-1} grating and focused on the sample by a toroidal mirror. The TEY and PFY data were acquired simultaneously using the sample current and a silicon drift detector (SDD) (TechnoAP), respectively. The SDD has an effective detection area of 50 mm^2 and a sample-detector distance of 25 mm. The angle between the SDD and the incident X-ray beam was set to 90°. Consequently, $\gamma = 90° - \alpha$.

The five samples (a CoO single crystal, a thin Li_2CO_3 layer on a NiO substrate, CoO powder, Co_3O_4 powder, and Li_2CO_3 powder) were measured. The CoO single crystal was mechanically polished with Al_2O_3 powder with a particle size of 0.05 µm. The Li_2CO_3 was deposited onto a 1000 nm-thick NiO film on a silicon wafer. It is hereafter denoted as Li_2CO_3/NiO. The thickness of the Li_2CO_3 thin film was 10 nm, determined by X-ray reflectivity measurements. CoO powder was purchased from Kojundo Chemical and stored under atmospheric conditions. A typical SEM (scanning electron microscopy) picture and particle size distribution by the light scattering are given in Figures S1 and S2 (Supplementary Material). SEM picture was obtained by JSM-7800F (JEOL). The CoO powder was put on the carbon conducting tape with extra powder removed. The particle size distribution was obtained using a laser scattering particle analyzer (LA-950V2, HORIBA). The CoO powder was dispersed in ethanol solution.

Li_2CO_3 powder was purchased from FUJIFILM Wako Pure Chemical. Co_3O_4 was prepared by the calcination of CoO at 800°C in air because the decomposition temperature of Co_3O_4 is 890°C in air [11]. The powder samples were put on the conductive tape. The extra powder particles were carefully removed not to create particle overlap. The acquired data were processed in the Athena software for background removal and normalization [12].

B. Voxel method

The voxel method is a numerical computational method in which the material body is divided into small cubes called voxels. Each voxel at the relative coordinate, $\vec{r} = (x, y, z)$, holds various parameters such as density, molar fraction, and composition, together with absorption coefficients for all of the component elements (Figure 1). To express the border more precisely, we introduce subvoxels with a smaller size, as shown in Figure 1(b), and calculate the absorption coefficients at the border. The sample was typically divided into 16 × 16 × 16 voxels and the voxel at the border was further divided into 8 × 8 × 8 subvoxels as shown in Figure 1(a, d). In the thin layer (10 nm thick Li_2CO_3) system the sample was divided into 32 × 32 × 32 voxels and then the voxel was divided into 8 × 8 × 8 subvoxels as shown in Figure 1(e) to calculate the borders more precisely. The calculation time depends on the number of divisions. For example, we need 8 times longer calculation time for the 32 × 32 × 32 voxels than that for the 16 × 16 × 16 voxels. Because the synchrotron radiation exhibits only a small amount of divergence, the light emitted from the storage ring is considered parallel. The voxel is placed with its edge parallel to the incident X-ray beam. The total fluorescence signal is calculated as

$$\begin{aligned} I_{\mathrm{F}} &= \int_{\vec{r}\in\Omega} \mathrm{d}I_{\mathrm{F}} \\ &= i_0 \int_{\vec{r}\in\Omega} k_X(\vec{r}) T_{\mathrm{in}}(\vec{r}, E) \mu_X(\vec{r}, E) T_{\mathrm{out}}(\vec{r}, E_{\mathrm{F}}) \mathrm{d}\vec{r} \\ &= i_0 \sum_{\vec{r}_n} k_X(\vec{r}_n) T_{\mathrm{in}}(\vec{r}_n, E) \mu_X(\vec{r}_n, E) v_n T_{\mathrm{out}}(\vec{r}_n, E_{\mathrm{F}}), \end{aligned} \quad (4)$$

where i_0, v_n, $T_{\mathrm{in}}(\vec{r}_n, E)$, and $T_{\mathrm{out}}(\vec{r}_n, E_{\mathrm{F}})$ are the incident X-ray intensity per unit area, the voxel volume (=l^3), and the transfer operators expressing the absorption of incident X-rays traveling through the sample to voxel n and the absorption of the outgoing X-rays from voxel n to the detector, respectively. Because the voxels are set with their side edges parallel to the incident X-rays (Figure 1), $T_{\mathrm{in}}(\vec{r}_n, E)$ can be simply expressed as

$$T_{\mathrm{in}}(\vec{r}_n, E) = \exp\left(- \sum_{so \text{ on } s\to r_n} \mu_{\mathrm{tot}}(r_{so}, E) l_{so} - \sum_{i \text{ on } s\to r_n} \mu_{\mathrm{tot}}(r_i, E) l \right),$$

where l and l_{so} are the edge lengths for a voxel and subvoxel, respectively, $\sum_{i \text{ on } s\to n}$ indicates the summation of all i-th voxels along the optical path from the source to the n-th voxel, and $\sum_{so \text{ on } s\to r_n}$ is similarly summed over the subvoxels along the optical path. However, $T_{\mathrm{out}}(\vec{r}_n, E_{\mathrm{F}})$ is somewhat complex because the outgoing fluorescence X-ray beam diverges and the X-rays travel to the detector in an oblique direction (Figure 1). The optical path length $l'_{j,r_n\xi}$ is not equal to the voxel edge length l; it depends on the fluorescence emission point, r_n, and the detection point of the detector, ξ. We use Siddon's algorithm to evaluate $l'_{j,r_n\xi}$ [13]. Similarly, we introduce $l'_{so,r_n\xi}$ as the optical path length in a subvoxel on the path:

$$T_{\mathrm{out}}(\vec{r}_n, E_{\mathrm{F}}) = \int_S \exp\left(- \sum_{j \text{ on } r_n\to\xi} \mu_{\mathrm{tot}}(r_j, E_{\mathrm{F}}) l'_{j,r_n\xi} - \sum_{so \text{ on } r_n\to\xi} \mu_{\mathrm{tot}}(r_{so}, E_{\mathrm{F}}) l'_{so,r_n\xi} \right) \mathrm{d}\xi,$$

where S is an individual detection area on the detector, and the integral is performed over all detection areas. In the calculation, $\mu_{\mathrm{tot}}(\vec{r}, E)$ is necessary: $\mu_{\mathrm{tot}}(\vec{r}, E) = \mu_{\mathrm{BG}}(\vec{r}, E) + \mu_X(\vec{r}, E)$. For each voxel, μ_{BG} can be evaluated using the Cromer–Liberman method [14].

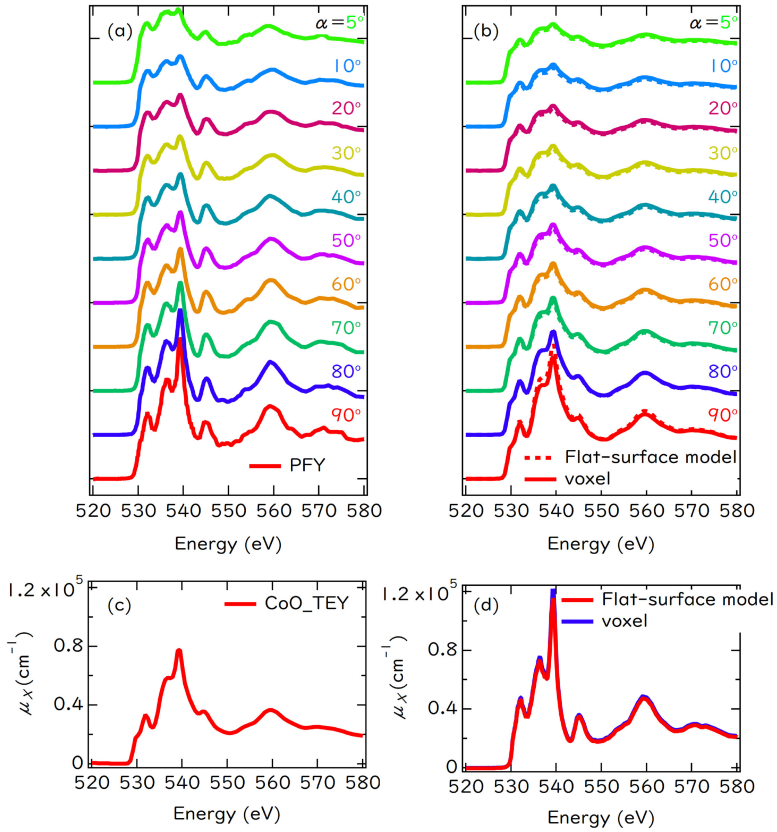

Figure 2: (a) PFY spectra of CoO single crystal. (b) Self-absorption-simulated spectra of CoO single crystal using its TEY spectrum. (c) TEY spectrum of CoO scaled by edge jump. (d) PFY spectra were corrected using the flat-surface model and the voxel method.

III. RESULTS AND DISCUSSION

A. CoO single crystal

To check the validity of the voxel method, we compared spectra constructed from experimental PFY-XAFS data for a flat CoO single crystal with those constructed from calculated data. The calculated PFY-XAFS spectra were obtained from TEY data after the background was removed and normalization was carried out. Figure 2(a) shows O K-edge PFY-XAFS spectra of the CoO single crystal for different incidence angles. Although CoO has a highly symmetric NaCl structure with oxygen atoms occupying the 4b sites and no polarization dependence is expected, we find a strong angular dependence. Especially for $\alpha = 5°$, all peaks are suppressed, which we attribute to the self-absorption effect. According to Eq. (1), when α becomes small, γ becomes nearly 90°. Consequently, the first term in the denominator of Eq. (1), $\mu_{\mathrm{tot}}(E)$ $[= \mu_{\mathrm{BG}}(E) + \mu_X(E)]$ becomes dominant and the $\mu_X(E)$ terms in the numerator and the denominator are canceled so that the peaks are strongly suppressed. However, for $\alpha = 90°$, the second term in the denominator becomes dominant and I_{F} is approximately proportional to μ_X, although the intensity is low because of the long path length for fluorescence X-rays.

Figure 2(b) shows the self-absorption-simulated spectra of CoO using Eq. (1) under the assumption that $\mu_X(E)$ is the same as that for the TEY-XAFS spectrum shown in Figure 2(c). We found the same behavior of the simulated and the observed spectra as shown in Figure 2(a, b). The self-absorption-simulated PFY-XAFS spectra at $\alpha = 5°$ are strongly affected while the self-absorption-simulated PFY-XAFS spectra at $\alpha = 90°$ appear similar to the original TEY-XAFS spectrum [Figure 2(b, c)]. The spectra in Figure 2(d) have been corrected using Eq. (1) (red line) from PFY-XAFS data acquired at an incidence angle of 50° and using the voxel method (blue line). Although small differences are observed in the peak intensities because of the finite size of the voxel, the spectrum corrected by the voxel method generally agrees well with that based on the flat-surface model [Eq. (1)], indicating that the voxel method calculation works well.

The PFY-XAFS structures appear clearer and sharper than the TEY-XAFS structures. Suppose the fluorescence XAFS data are acquired with high energy resolution (less than 1 eV). In that case, high-energy-resolution XAFS spectra are expected, which is known as the high-energy-resolution fluorescence detection (HERFD) method. However, we used an SDD in this work, which has an energy resolution of 80 eV [15]. Thus, the SDD's energy resolution is insufficient to produce a HERFD spectrum. We speculate that the surface of the polished single crystal was somewhat oxidized or reconstructed. These effects were detected in the surface-sensitive TEY-XAFS spectra.

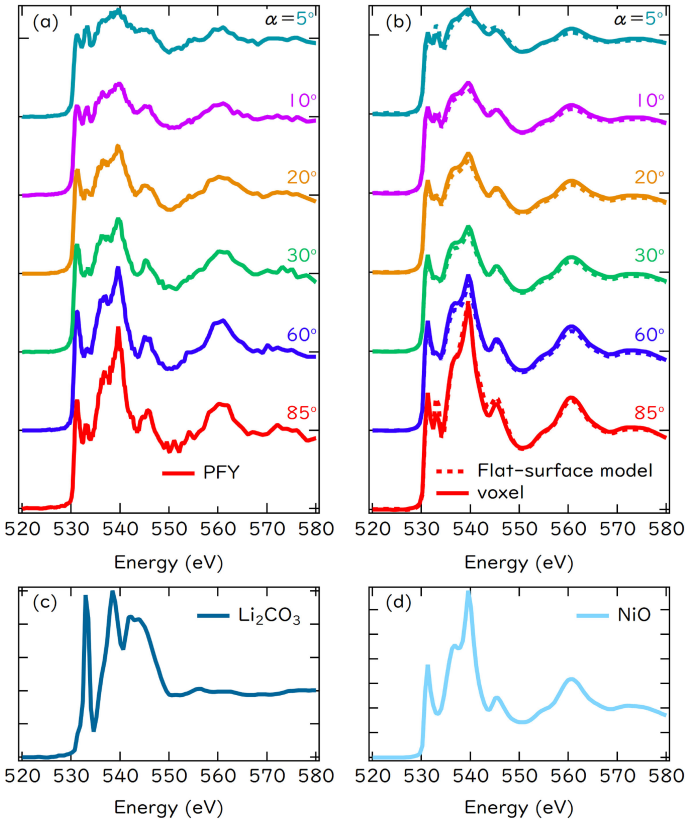

Figure 3: (a) PFY spectra of Li_2CO_3/NiO film. (b) Self-absorption-simulated spectra of Li_2CO_3/NiO film, as calculated from TEY. TEY-XAFS spectra of (c) Li_2CO_3 powder and (d) a NiO single crystal.

B. Li_2CO_3/NiO film

We tested the performance of the voxel method in a mixed Li_2CO_3/NiO system containing several components. For the layer-on-layer flat surface, the fluorescence signal I_F is given in Eq. (5), where O fluorescence is emitted from each layer of the sample:

$$
\begin{aligned}
I_F = & \frac{k_{1X} I_0 \mu_{1X}(E)}{\mu_{1\mathrm{tot}}(E) + \mu_{1\mathrm{tot}}(E_F)\frac{\sin\alpha}{\sin\gamma}} \\
& \times \left[1 - \exp\left(-\frac{\mu_{1\mathrm{tot}}(E)}{\sin\alpha} d_1 - \frac{\mu_{1\mathrm{tot}}(E_F)}{\sin\gamma} d_1\right)\right] \\
& + \exp\left(-\frac{\mu_{1\mathrm{tot}}(E)}{\sin\alpha} d_1 - \frac{\mu_{1\mathrm{tot}}(E_F)}{\sin\gamma} d_1\right) \\
& \times \frac{k_{2X} I_0 \mu_{2X}(E)}{\mu_{2\mathrm{tot}}(E) + \mu_{2\mathrm{tot}}(E_F)\frac{\sin\alpha}{\sin\gamma}} \\
& \times \left[1 - \exp\left(-\frac{\mu_{2\mathrm{tot}}(E)}{\sin\alpha} d_2 - \frac{\mu_{2\mathrm{tot}}(E_F)}{\sin\gamma} d_2\right)\right].
\end{aligned}
\tag{5}
$$

The upper Li_2CO_3 film with a thickness d_1 (= 10 nm) is denoted as **1** and the NiO substrate with a thickness d_2 (= 1000 nm) is denoted as **2**.

Equation (5) is composed of two terms. The first term is the fluorescence signal from the thin overlayer **1**, and the second term is that for the thick substrate film **2** after absorption of incident X-rays and emission of fluorescence by the overlayer **1**. Because oxygen atoms are present in both films, the I_F signal is generated in a complex manner via interference between **1** and **2**.

Figure 3(a) shows the observed O K-absorption edge PFY-XAFS spectra of Li_2CO_3/NiO acquired at different incidence angles. Figure 3(c, d) shows a TEY-XAFS spectrum of Li_2CO_3 powder and a reference NiO single crystal. The raw PFY-XAFS spectrum is similar to the TEY-XAFS spectrum of the NiO single crystal [Figure 3(d)]. The angular dependence of the PFY-XAFS spectrum can be understood based on the PFY-XAFS spectra of the CoO single-crystal. When α is small, the PFY-XAFS spectra are strongly distorted, whereas a weaker self-absorption effect is observed when $\alpha \sim 90°$. However, an extra peak appears at 533 eV when $\alpha = 5°$ and 85°. By comparison of the spectra with the TEY-XAFS spectrum of Li_2CO_3 powder, we assign this to the π^* peak of CO_3^{2-} in Li_2CO_3. The appearance of the peak in the $\alpha = 85°$ spectrum can be understood from the following term in Eq. (5):

$$
\exp\left(-\frac{\mu_{1\mathrm{tot}}(E)}{\sin\alpha} d_1 - \frac{\mu_{1\mathrm{tot}}(E_F)}{\sin\gamma} d_1\right). \tag{6}
$$

In Eq. (6), the first and second terms represent absorption of incident X-rays by the thin overlayer **1** and absorption of the outgoing X-ray fluorescence emitted from the substrate **2** by the thin overlayer **1**, respectively. For $\alpha = 5°$, the first term acts as previously described, whereas at $\alpha = 85°$, the second term reduces the fluorescence signal from the substrate **2**. As

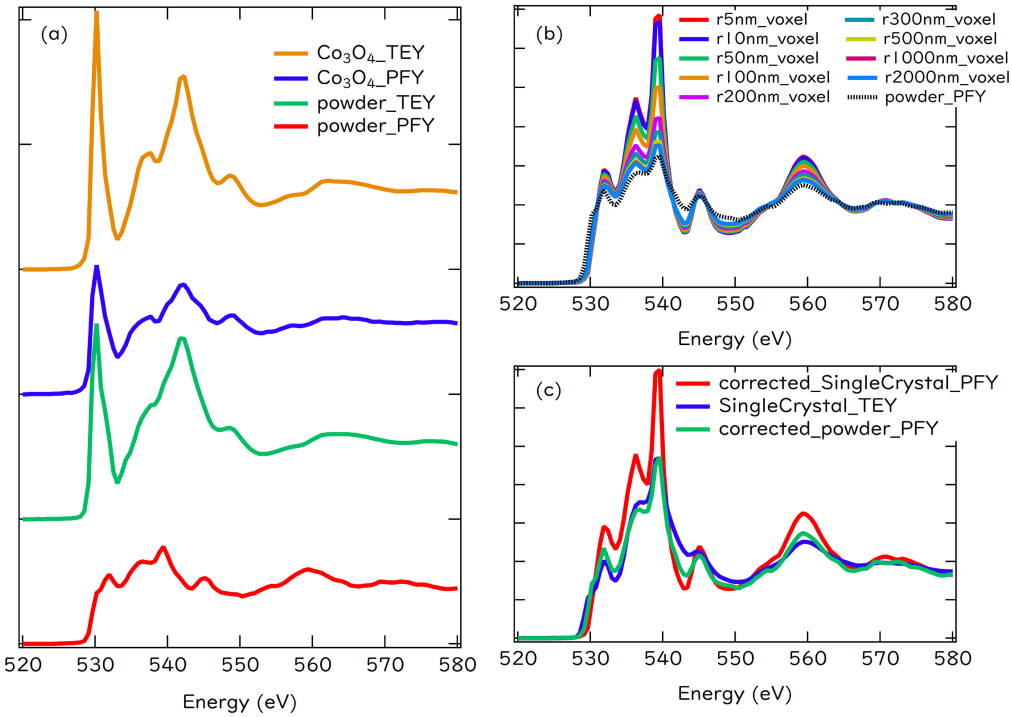

Figure 4: (a) Experimental spectra (TEY and PFY) of Co_3O_4 and CoO powders. (b) Self-absorption-simulated spectra of CoO with different particle sizes, as calculated using the voxel method. A sphere with radius r is assumed. (c) Corrected PFY-XAFS spectra of the powder and single crystal of CoO and the TEY-XAFS spectrum of the single crystal of CoO.

a result, the contribution from the substrate **2** is reduced for both $\alpha = 5°$ and 85°.

Figure 3(b) shows the self-absorption-simulated spectra using the voxel method and Eq. (5). We estimated the μ_X values for the Li_2CO_3 powder and NiO from their TEY-XAFS spectra shown in Figure 3(c, d). We assumed that k_{1X} and k_{2X} were equal and that O was homogeneously distributed in each film. The solid and dotted lines in Figure 3(b) correspond to the simulated spectra obtained by the voxel method and the flat-surface model, respectively. The spectral trend are roughly reproduced by both methods. In the voxel method, the fitting is not so good in a low α region because of the limitation of the machine power not to make the further smaller subvoxel.

C. CoO powder

Finally, we analyze the PFY-XAFS spectra of CoO powder by the voxel method. Figure 4(a) shows TEY-XAFS and PFY-XAFS spectra of Co_3O_4 and CoO powders. The TEY-XAFS and PFY-XAFS spectra of Co_3O_4 exhibit similar features and correspond well with the spectrum in the literature [16]. The PFY-XAFS spectra of Co_3O_4 have lower peak intensities than the corresponding TEY-XAFS spectra, reflecting the effect of self-absorption.

The TEY-XAFS spectrum of the CoO powder is similar to that of Co_3O_4, indicating that surface of the CoO powder sample is oxidized to Co_3O_4. Compared with the TEY-XAFS spectrum of the CoO powder, the PFY-XAFS spectrum is more similar to the TEY-XAFS of a CoO single crystal.

Figure 4(b) shows the self-absorption-simulated spectra of CoO powder with various sizes using the voxel method. We assumed a single spherical particle. The μ_X used for the simulation was estimated from the PFY-XAFS spectrum of CoO single crystal after self-absorption correction [Figure 2(d)]. For a particle with a radius of ~10 nm, the self-absorption-simulated spectrum is unaffected by self-absorption. In Eq. (1) for the flat-surface model, the term $1 - \exp\left(-\frac{\mu_{tot}(E)}{\sin\alpha}d - \frac{\mu_{tot}(E_F)}{\sin\gamma}d\right)$ can be approximated as $\left(-\frac{\mu_{tot}(E)}{\sin\alpha}d - \frac{\mu_{tot}(E_F)}{\sin\gamma}d\right)$ and is canceled by the denominator. When the particle radius is greater than 500 nm, the self-absorption-simulated spectrum no longer varies with particle size, indicating saturation of the self-absorption effect, which corresponds to Eq. (3) in the flat-surface model. The particle size of CoO powder was about a 2–20 μm as shown in Figure S1 and its average size determined by light scattering was 7 μm in Figure S2 (Supplementary Material). Consequently, we can consider the self-absorption effect of the PFY signal as saturated.

Figure 4(c) shows the spectrum after self-absorption correction assuming a particle radius of 1000 nm. This spectrum agrees well with the TEY-XAFS spectrum of the CoO single crystal. The peak intensities are reduced compared with those in the PFY-XAFS spectrum of the CoO single crystal after self-absorption correction. This difference is due to the presence of a Co_3O_4 thin layer on the surface, which is observed in the TEY-XAFS of the CoO powder.

We performed calculations for different thicknesses of the Co_3O_4 shell around the CoO core. Figure 5(a) shows the self-absorption-simulated spectra of CoO particles with core radii of 100, 500, and 1000 nm, where the particles are covered

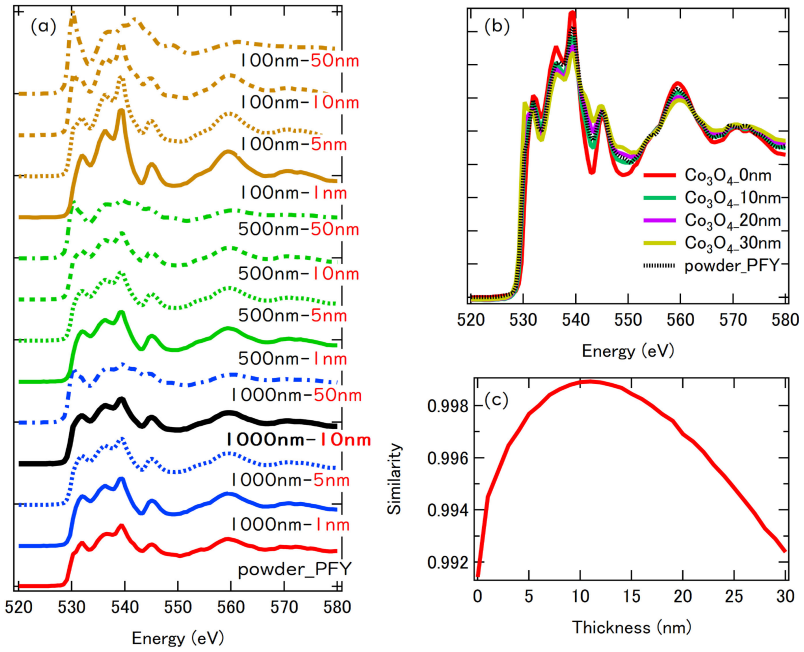

Figure 5: (a) Self-absorption-simulated spectra of particles with CoO core radii of 100, 500, and 1000 nm, where the cores are coated with Co_3O_4. The labels in the figure for example, 100 nm–50 nm mean the CoO core with 100 nm raius covered with 50 nm thick Co_3O_4 shell. (b) Self-absorption-simulated spectra of CoO samples with various thicknesses. (c) Pearson correlation coefficient between the PFY spectrum of CoO powder and the self-absorption-simulated spectra with a model of a CoO core coated with Co_3O_4 shell.

with a Co_3O_4 shell with different thicknesses. The overall degree of self-absorption changes with the CoO core radius, whereas the shape of the spectra changes with the thickness of the Co_3O_4 shell. The PFY-XAFS spectrum of the CoO powder is well reproduced by a CoO core with a radius of 1000 nm covered with a Co_3O_4 shell with a thickness of less than 50 nm. We performed calculations with the radius of the CoO core set at 1000 nm and with the thickness of the Co_3O_4 shell varied in 10 nm steps. As shown in Figure 5(b), the spectrum of CoO with a thickness of 10 nm agrees with the PFY-XAFS spectrum of the CoO powder. We evaluated the similarity of the two spectra using the Pearson correlation coefficient ($= \frac{\mathrm{cov}[XY]}{\sigma_X \sigma_Y}$), where cov[$XY$] and σ_X σ_Y are the covariance and standard deviation of spectra X and Y, respectively. Figure 5(c) shows the similarity of the spectra, indicating that the Co_3O_4 shell thickness is approximately 10 ± 5 nm. This result is reasonable considering the TEY measurement depth (~5 nm [17]).

D. Fluorescence XAFS for bulk measurements in the soft X-ray region

XAFS is an important technique for the analysis of local structure. In the hard X-ray region, the advantage of XAFS is its deep penetration ability, which enables easy transmission-mode acquisition of the structural information about the bulk region of a sample. In contrast, transmission-mode XAFS in the soft X-ray region is difficult to carry out because it requires a special device and windows to prepare a thin and homogeneous sample [18]. TEY-XAFS is usually used; however, it is still surface sensitive. Its sampling depth is less than 10 nm for an X-ray energy of <1000 eV [17, 19]. The difference in surface composition from the bulk strongly affects the spectra and gives erroneous results. Because PFY-XAFS can be used to detect deeper regions, PFY-XAFS measurements are more suitable for acquiring bulk data in the soft X-ray region. In addition, recently HERFD-XANES (X-ray absorption near edge structure) method has rapidly been developed, which provides high-energy-resolution XANES spectra and fruitful information about the electronic states of samples [20–26]. HERFD-XANES uses a fluorescence detection and strongly suffers from the self-absorption effect if one measures the thick concentrated samples. It is difficult to obtain the HERFD-XANES of reference compounds without self-absorption correction. Thus, the HERFD-XANES method necessitates the self-absorption correction. In the hard X-ray region, the flat-surface method using Eq. (1) is available using a flat disc sample prepared by compacting a sample powder and the sample roughness is expected to have a negligible influence. In the soft X-ray region, Eq. (1) is limited because of surface roughness and inhomogeneity in the powder sample. The voxel method proposed here is useful for the analysis of powder systems to express the roughness and inhomogeneity in the sample more precisely. We can obtain information about the sample composition and roughness by SEM, electron-probe micro-analysis (EPMA) and atomic force microscopy (AFM). As shown in Section III.C, the TEY-XAFS measurement is preferably conducted simultaneously with PFY-XAFS to detect surface contaminants and compositions. The voxel method is still limited due to the high computational cost. It took 30 min for a Windows computer with i7-6700HQ CPU (clock = 2.6 GHz) to calculate the 16 × 16 × 16 voxels. We

have to calculate many self-absorption-simulated spectra repeatedly with different physical parameters such as the thickness of the surface layers and compare them with the observed one to estimate the self-absorption correction. Thus, we spent a few weeks to obtain the final corrected spectra under the appropriate model structure. However, the improvement of the program and the increase in the computer's calculation machine power will allow more realistic calculations, and the voxel method will make the PFY-XAFS a powerful and practical bulk analysis tool in the soft X-ray region.

IV. CONCLUSION

The voxel method enables us to correct for self-absorption of PFY-XAFS for a sample with an arbitrary shape. Once the sample roughness, composition, distribution, and morphology are known, the PFY-XAFS data can be corrected even for inhomogeneous samples. We can determine the bulk information in the soft X-ray region using PFY-XAFS. Empowered by the HERFD technique, PFY-XAFS will be a more conventional and powerful analysis tool in the soft X-ray regions.

Acknowledgments

This study is supported by the New Energy and Industrial Technology Development Organization (NEDO; Grant No. JPNP21006). The authors thank FORTE Science Communications (https://www.forte-science.co.jp/) for editing the English language.

Appendix

The SEM and light scattering data of CoO powder are available in Supplementary Material at https://doi.org/10.1380/ejssnt.2025-010.

References

[1] Y. Iwasawa, K. Asakura, and M. Tada (Eds.), *XAFS Techniques for Catalysts, Nanomaterials, and Surfaces* (Springer Cham, 2017).
[2] C. T. Chantler, F. Boscherini, and B. Bunker (Eds.), *International Tables for Crystallography*, Vol. 1 (John Wiley & Sons, 2024).
[3] T. Kawai, K. K. Bando, Y.-K. Lee, S. T. Oyama, W.-J. Chun, and K. Asakura, J. Catal. **241**, 20 (2006).
[4] J. H. Hubbell and S. M. Seltzer, *Tables of X-Ray Mass Attenuation Coefficients and Mass Energy-Absorption Coefficients 1 keV to 20 MeV for Elements Z = 1 to 92 and 48 Additional Substances of Dosimetric Interest*, NISTIR 5632 (National Institute of Standards and Technology, Gaithersburg, MD, 1995).
[5] T. Ohta, *Chemical Applications of Synchrotron Radiation* (World Scientific, 2002) p. 664.
[6] K. Nakanishi and T. Ohta, *Advanced Topics in Measurements* (IntechOpen, 2012).
[7] Z. Tan, J. I. Budnick, and S. M. Heald, Rev. Sci. Instrum. **60**, 1021 (1989).
[8] L. Tröger, D. Arvanitis, K. Baberschke, H. Michaelis, U. Grimm, and E. Zschech, Phys. Rev. B **46**, 3283 (1992).
[9] A. Iida and T. Noma, Jpn. J. Appl. Phys. **32**, 2899 (1993).
[10] K. Asakura, in *XAFS Techniques for Catalysts, Nanomaterials, and Surfaces*, edited by Y. Iwasawa, K. Asakura, and M. Tada (Springer Cham, 2017) p. 193.
[11] V. Bartůněk, S. Huber, D. Sedmidubský, Z. Sofer, P. Šimek, and O. Jankovský, Ceram. Int. **40**, 12591 (2014).
[12] B. Ravel and M. Newville, J. Synchrotron Radiat. **12**, 537 (2005).
[13] R. L. Siddon, Med. Phys. **12**, 252 (1985).
[14] D. T. Cromer and D. A. Liberman, Acta Crystallogr. A **37**, 267 (1981).
[15] C. Yogi, H. Ishii, K. Nakanishi, I. Watanabe, K. Kojima, and T. Ohta, Mem. SR Cent. Ritsumeikan Univ. **14** (2012).
[16] S. Kenmoe, D. H. Douma, A. T. Raji, B. M'Passi-Mabiala, T. Götsch, F. Girgsdies, A. Knop-Gericke, R. Schlögl, and E. Spohr, Nanomaterials **12**, 921 (2022).
[17] M. Balasubramanian, H. S. Lee, X. Sun, X. Q. Yang, A. R. Moodenbaugh, J. McBreen, D. A. Fischer, and Z. Fu, Electrochem. Solid-State Lett. **5**, A22 (2002).
[18] M. Nagasaka, H. Yuzawa, and N. Kosugi, J. Electron Spectrosc. Relat. Phenom. **200**, 293 (2015).
[19] B. H. Frazer, B. Gilbert, B. R. Sonderegger, and G. De Stasio, Surf. Sci. **537**, 161 (2003).
[20] P. Glatzel, M. Sikora, S. G. Eeckhout, O. V. Safonova, G. Smolentsev, G. Pirngruber, J. A. van Bokhoven, J.-D. Grunewaldt, and M. Tromp, AIP Conf. Proc. **879**, 1731 (2007).
[21] M. Bauer, Phys. Chem. Chem. Phys. **16**, 13827 (2014).
[22] H. Asakura and T. Tanaka, Chem. Lett. **50**, 1075 (2021).
[23] H. Asakura, M. Konno, N. Kawamura, S. Hosokawa, K. Teramura, and T. Tanaka, J. Phys. Chem. C **127**, 24192 (2023).
[24] K. Dong, B. Hu, M. H. A. Rashid, B. Lu, K. Miyabayashi, K. Higashi, T. Uruga, Y. Iwasawa, D. Kido, S. Takakusagi, and K. Asakura, e-J. Surf. Sci. Nanotechnol. **22**, 129 (2024).
[25] C. H. Booth and F. Bridges, Phys. Scr. **2005**, 202 (2005).
[26] R. M. Trevorah, C. T. Chantler, and M. J. Schalken, IUCrJ **6**, 586 (2019).